Uncertainty Analysis of Soil Moisture and Vegetation Indices Using Aquarius Scatterometer Observations

Kaighin Alexander McColl, *Student Member, IEEE*, Dara Entekhabi, *Senior Member, IEEE*, and María Piles, *Member, IEEE*

Abstract—Simple functions of radar backscatter coefficients have been proposed as indices of soil moisture and vegetation, such as the radar vegetation index, i.e., RVI, and the soil saturation index, i.e., m_s. These indices are ratios of noisy and potentially miscalibrated radar measurements and are therefore particularly susceptible to estimation errors. In this study, we consider uncertainty in satellite estimates of RVI and m_s arising from two radar error sources: noise and miscalibration. We derive expressions for the variance and bias in estimates of RVI and m_s due to noise. We also derive expressions for the sensitivity of RVI and m_s to calibration errors. We use one year (September 1, 2011 to August 31, 2012) of Aquarius scatterometer observations at three polarizations (σ_{HH}, σ_{VV}, and σ_{HV}) to map predicted error estimates globally, using parameters relevant to the National Aeronautics and Space Administration Soil Moisture Active and Passive satellite mission. We find that RVI is particularly vulnerable to errors in the calibration offset term over lightly vegetated regions, resulting in overestimates of RVI in some arid regions. m_s is most sensitive to calibration errors over regions where the dynamic range of the backscatter coefficient is small, including deserts and forests. Noise induces biases in both indices, but they are negligible in both cases; however, it also induces variance, which is large for highly vegetated regions (for RVI) and areas with low dynamic range in backscatter values (for m_s). We find that, with appropriate temporal and spatial averaging, noise errors in both indices can be reduced to acceptable levels. Areas sensitive to calibration errors will require masking.

Index Terms—Aquarius/SAC-D, microwave remote sensing, radar vegetation index (RVI), scatterometer, Soil Moisture Active Passive (SMAP), soil moisture, soil saturation index, uncertainty analysis.

I. Introduction

SIMPLE functions of radar backscatter coefficients have been proposed as indices of soil moisture and vegetation. Compared to retrievals of biomass and soil moisture obtained from inverting electromagnetic scattering models, these indices

are simple to apply, do not require ancillary data, and possess vastly fewer tuning parameters, if any. Two such indices are applicable to the Soil Moisture Active and Passive (SMAP) mission [1]. Planned for launch in September 2014, SMAP will provide global mapping of radar backscatter and brightness temperature at L-band. The radar vegetation index (RVI) [2] has been proposed for use in estimating vegetation properties relevant to radar-only soil moisture retrieval algorithms. The soil saturation index, i.e., m_s, of Wagner *et al.* [3] is an optional radar-only soil moisture algorithm [4]. While neither index is part of the SMAP baseline algorithm suite, they are important research products that can be generated by the SMAP mission instrument measurements of backscatter cross section.

Both the RVI and m_s are ratios of noisy radar measurements and are therefore particularly susceptible to estimation errors. Furthermore, they are also susceptible to biases due to imperfect calibration of the radar backscatter coefficients and index-specific parameters. Understanding the sensitivity and robustness of soil moisture and vegetation indices to these errors is essential prior to their use by satellite missions such as SMAP. However, few studies have quantified their impacts. Error analysis of m_s is considered in [5] and [6]. A first-order error propagation equation is used to estimate the variance of m_s. However, they do not consider the impact of noise on biases in m_s. No uncertainty analysis studies exist for RVI.

In this paper, we consider uncertainty in satellite estimates of RVI and m_s arising from two radar error sources: noise and miscalibration. We consider these error sources independently. In Section II, we describe the Aquarius data set used in this study, define and review RVI and m_s, and introduce our uncertainty analysis methodology. In Section III, we present the results of the analysis. In the final section, we describe the main findings of this paper and consider their implications for the upcoming SMAP mission.

II. Data and Methods

Here, we describe the Aquarius data set used to estimate index uncertainty globally. We describe the radar vegetation and soil moisture indices considered in this study. Finally, we derive metrics for estimating variance and bias in each index due to radar noise and for estimating the sensitivity of each metric to calibration errors.

A. Global Aquarius Data

The NASA/SAC-D Aquarius mission provides global observations of sea surface salinity using collocated active and

This article has been accepted for inclusion in a future issue of this journal. Content is final as presented, with the exception of pagination.

2   IEEE TRANSACTIONS ON GEOSCIENCE AND REMOTE SENSING

passive L-band observations. Launched in June 2011, it crosses the equator twice per day, at 6 A.M. (descending) and 6 P.M. (ascending), with a repeat time of seven days. Its payload includes a 1.26-GHz scatterometer, with three beams arranged in a pushbroom configuration at incidence angles of 28.7° (inner beam), 37.8° (middle beam), and 45.6° (outer beam). The scatterometer's individual footprints are ellipses with principal axis dimensions slightly smaller than those of the collocated radiometer (76×94, 84×120, and 96×156 km, respectively). The overall swath width is 390 km [7].

In this study, we use one year (September 1, 2011 to August 31, 2012) of version 2.0 Aquarius observations of normalized radar backscatter cross section at three polarizations (σ_{HH}, σ_{VV}, and σ_{HV}). Since the Aquarius data are still undergoing calibration and the final calibrated data may be different to those currently available, in this study, we specifically and additionally analyze the impact of calibration offsets (see Section II-D2). Only observations from the middle beam (37.8°) are used since this is closest to the fixed SMAP incidence angle (40°). Quality flags supplied with the data have been used to screen out Aquarius maneuvers and regions contaminated by RFI. Furthermore, observations either fully or partially overlapping ocean or water bodies were removed. Observations over Antarctica and Greenland were also removed since regions dominated by snowcover are not relevant for this study. To preserve the instrument's spatial resolution, we gridded the data at the footprint scale. However, since Aquarius footprints do not exactly overlap on repeat, a modified sampling approach was required (see Fig. 1 for a schematic). The first seven days of footprints were used to define a grid (the red circle in Fig. 1). All subsequent observations with centers less than 0.05° from a grid center are included in that cell (e.g., black circle in Fig. 1). Otherwise, they are excluded (e.g., black dashed circle in Fig. 1). Note that this scheme results in some footprints being included in multiple grid cells, whereas others are not included in any cells. Our choice of a gridding threshold (0.05°) results in $> 95\%$ of the Aquarius data being used.

B. RVI

The RVI is a measure of volume scattering typically caused by structural elements of vegetation canopies (e.g., branches), which is first defined in [8]. It is given by

$$\text{RVI} = \frac{8\sigma_{\text{HV}}}{\sigma_{\text{HH}} + \sigma_{\text{VV}} + 2\sigma_{\text{HV}}}. \tag{1}$$

All backscatter coefficients in this study are in linear units, unless otherwise specified. RVI varies between 0 and 1, increasing with vegetation cover. It can theoretically be shown to be a measure of volume scattering from a cloud of randomly oriented thin cylinders [2]; this is a common representation used for vegetation canopies in more complex radar retrieval algorithms (e.g., [9] and [10]). As such, RVI is simple yet grounded in scattering theory and is a promising metric for measuring vegetation cover. In particular, it is a measure of vegetation structure that is independent of vegetation greenness, a property measured by other indices such as the normalized difference vegetation index. RVI has been used in a wide
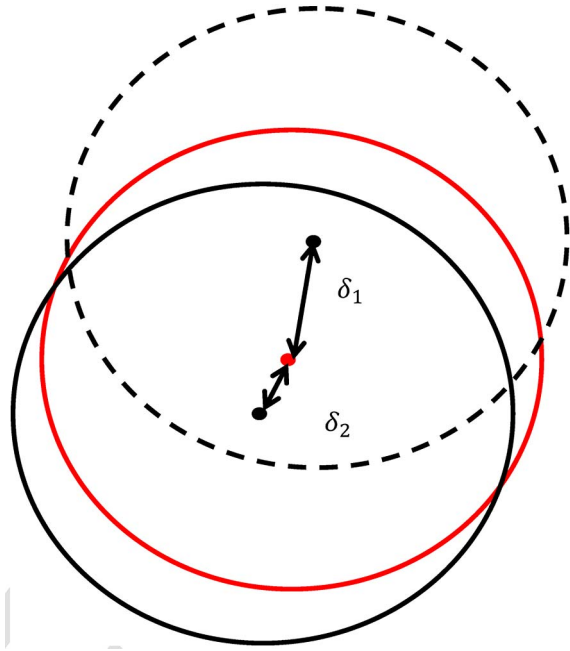

Fig. 1. Schematic of the sampling method used to grid Aquarius data. Footprints with centers less than a threshold (0.05° in this study) from the grid cell's center are included in the grid cell (red). Here, $\delta_2 < 0.05°$; thus, the corresponding footprint is included in the grid cell (solid black); $\delta_1 > 0.05°$; thus, the corresponding footprint is excluded (dashed black).

range of applications, including classifying regions susceptible to landslides [11] and tracking lava flows [12]. It has been proposed for use in more complex radar soil moisture retrieval algorithms by classifying vegetation cover in a region as low, medium, or high [13], [14]. This allows less general and less computationally intensive retrieval algorithms to be subsequently deployed. A further advantage for SMAP is that RVI is based on radar observations; thus, RVI estimates are temporally and spatially collocated with radar-derived soil moisture estimate. This avoids representativeness errors incurred from using ancillary data from other observing systems.

C. Soil Saturation Index m_s

Wagner *et al.* [3] used a change-detection approach to estimate soil moisture using radar observations. They introduced an index m_s for estimating the degree of soil saturation in a thin layer of surface soil, which is defined as

$$m_s(t) = \frac{\sigma^{0,\,\text{dB}}(40, t) - \sigma_{\text{dry}}^{0,\,\text{dB}}(40, t)}{\sigma_{\text{wet}}^{0,\,\text{dB}}(40, t) - \sigma_{\text{dry}}^{0,\,\text{dB}}(40, t)}$$

where $\sigma^{0,\,\text{dB}}(40, t)$ is the backscatter coefficient (in decibels) at a 40° incidence angle at time t; and $\sigma_{\text{dry}}^{0,\,\text{dB}}(40, t)$ and $\sigma_{\text{wet}}^{0,\,\text{dB}}(40, t)$ are the values observed when the soil is totally dry and fully saturated, respectively. We use the superscript "dB" to emphasize the different units compared with those used in RVI. An exponential filter can be applied to m_s to estimate the profile soil moisture, such as that used in the soil water index [15]. Comparisons of m_s with an soil moisture and ocean salinity-derived soil saturation index yielded broadly consistent

This article has been accepted for inclusion in a future issue of this journal. Content is final as presented, with the exception of pagination.

MCCOLL *et al.*: UNCERTAINTY ANALYSIS OF SOIL MOISTURE AND VEGETATION INDICES 3

results [16]. The original formulation uses observations from the European Remote Sensing satellite scatterometer, taken over a range of incidence and azimuth angles, requiring further processing to normalize the observations to the same $40°$ incidence angle using time series of backscatter coefficients. Since we use Aquarius observations taken at a single incidence angle, we do not consider these corrections. Furthermore, real-time soil moisture observations considered in [3] require estimates of $\sigma_{\text{wet}}^{0,\text{ dB}}(40, t)$ and $\sigma_{\text{dry}}^{0,\text{ dB}}(40, t)$ to vary with time, to account for the effects of seasonally varying vegetation. Since these variations are typically small and we only consider soil moisture climatology, we do not apply these corrections. Assuming that over a sufficiently long time series both fully dry and saturated conditions will occur, $\sigma_{\text{dry}}^{0,\text{ dB}}$ and $\sigma_{\text{wet}}^{0,\text{ dB}}$ can be estimated by the minimum and maximum observed backscatter coefficients, respectively. The resulting formulation used in this study is

$$m_s(\sigma_{\text{VV}}) = \frac{10\log_{10}(\sigma_{\text{VV}}) - \sigma_{\text{VV}}^{\text{min, dB}}}{\sigma_{\text{VV}}^{\text{max, dB}} - \sigma_{\text{VV}}^{\text{min, dB}}} \qquad (2)$$

where we have altered the expression to be a function of σ_{VV} in linear units. We drop the angle and time dependence terms for brevity. While σ_{HH} is known to be more sensitive to soil moisture, we define m_s as a function of σ_{VV} to be consistent with previous studies, which only had access to vertically copolarized backscatter coefficients (e.g., [5]). m_s varies between 0 and 1. The volumetric soil moisture can be obtained by multiplying m_s by the soil porosity. In this study, we calculate the maximum and minimum backscatter coefficients from the one year of data available. One year of observations is not necessarily sufficient to observe both completely dry and saturated conditions at all locations; we discuss the accuracy of this assumption later in this paper. In arid regions, where the soil never reaches saturation, a bias correction factor must be applied to $\sigma_{\text{VV}}^{\text{max, dB}}$ (e.g., [17]).

D. Error Analysis

Here, we derive expressions for the variance and bias in estimates of RVI and m_s due to noise. We also derive expressions for the sensitivity of RVI and m_s to calibration errors.

1) Noise Errors: Radar backscatter cross-section observations include noise present in both the instrument and the observed scene [18]. Noise is generated by various sources, including instrument characteristics, data processing, and spatial inhomogeneities. Noise is summarized by the K_p parameter, i.e., the normalized standard deviation of the observation measurement error, given by

$$K_{p_{pq}} = \sqrt{\frac{1}{N_{\text{looks}}}\left(1 + \frac{2}{\text{SNR}_{pq}} + \frac{1}{\text{SNR}_{pq}^2}\right)}$$

where $pq = \{\text{HH, VV, HV, VH}\}$, N_{looks} is the number of looks, and SNR is the signal-to-noise ratio, which is defined as

$$\text{SNR}_{pq} = \frac{\sigma_{pq}^{\text{signal}}}{\sigma_{pq}^{\text{noise floor}}}.$$

For SMAP, N_{looks} varies along the swath, reaching a minimum at the swath's inner edge (150-km cross-track distance). Therefore, K_p is greatest at the inner edge of the swath, for scenes where the average backscatter is equal to the noise floor $\sigma^{\text{noise floor}}$. For SMAP, the designated noise floor is -25 dB, and the K_p error budget allocation is 0.72 dB. Following standard practice for scatterometer measurements, the latter quantity refers to $10\log_{10}(1 + K_p)$ [19]; converting this value to linear units gives a K_p of 0.18. In this study, we use this value as an estimate for both $K_{p_{pp}}$ and $K_{p_{pq}}$. Note that these are very conservative estimates. In comparison, of the 2 835 326 individual Aquarius observations used in this study, the median Aquarius K_p values for σ_{HH}, σ_{VV}, and σ_{HV} are 0.01, 0.01, and 0.06, respectively. Almost all (99.99% and 91.79% of the cross- and copolarized observations, respectively) had K_p values less than 0.18.

A standard error model for radar backscatter cross sections in the presence of noise is given by

$$\sigma_{pp_0} = \sigma_{pp}(1 + K_{p_{pp}}\omega)$$
$$\sigma_{pq_0} = \sigma_{pq}(1 + K_{p_{pq}}\omega)$$

where $\omega \sim N(0, 1)$; and σ_{HH_0}, σ_{HV_0}, and σ_{VV_0} are noisy measurements. By Taylor expansion of the observed RVI around the true value, analytical approximations for the mean bias and standard error of RVI estimates are obtained. The expected value of RVI in the presence of noise is

$$E(\text{RVI}_0) \approx \text{RVI} + \frac{K_{p_{pp}}^2 \text{RVI}^3}{64\sigma_{\text{HV}}^2}(\sigma_{\text{HH}} + \sigma_{\text{VV}})^2$$

$$+ \frac{K_{p_{pq}}^2 \text{RVI}^2}{4}\left(\frac{\text{RVI}}{4} - 1\right) + \frac{K_{p_{pp}}K_{p_{pq}}\text{RVI}^2}{8\sigma_{\text{HV}}}$$

$$\times \left(\frac{\text{RVI}}{2} - 1\right)(\sigma_{\text{HH}} + \sigma_{\text{VV}}).$$

The terms beyond RVI are a mean bias in RVI_0 induced by noise in the backscatter observations. The variance of RVI, which is useful in quantifying the standard error, is

$$\text{Var}(\text{RVI}_0)$$

$$\approx \left(K_{p_{pq}}\text{RVI}\left(1 - \frac{\text{RVI}}{4}\right) - \frac{K_{p_{pp}}\text{RVI}^2}{8\sigma_{\text{HV}}}(\sigma_{\text{HH}} + \sigma_{\text{VV}})\right)^2$$

$$+ 2\left(\frac{K_{p_{pp}}^2 \text{RVI}^3}{64\sigma_{\text{HV}}^2}(\sigma_{\text{HH}} + \sigma_{\text{VV}})^2 + \frac{K_{p_{pp}}K_{p_{pq}}\text{RVI}^2}{8\sigma_{\text{HV}}}\right.$$

$$\times \left(\frac{\text{RVI}}{2} - 1\right)(\sigma_{\text{HH}} + \sigma_{\text{VV}})$$

$$\left. + \frac{K_{p_{pq}}^2 \text{RVI}^2}{4}\left(\frac{\text{RVI}}{4} - 1\right)\right)^2. \qquad (3)$$

Appendix A includes the derivation of these statistics. Similar analyses for m_s yield

$$E(m_{s_0}) \approx m_s - \frac{5K_p^2}{\ln(10)\left(\sigma_{\text{VV}}^{\text{max, dB}} - \sigma_{\text{VV}}^{\text{min, dB}}\right)} \qquad (4)$$

$$\text{Var}(m_{s_0}) \approx \left(\frac{10}{\ln(10)\left(\sigma_{\text{VV}}^{\text{max, dB}} - \sigma_{\text{VV}}^{\text{min, dB}}\right)} \right)^2 \left(K_p^2 + \frac{K_p^4}{2} \right).$$

(5)

Appendix B contains the step-by-step derivations.

2) Calibration Errors: Radar backscatter observations must be calibrated before use, using targets with known scattering properties. In addition, for m_s, $\sigma_{\text{VV}}^{\text{min, dB}}$ and $\sigma_{\text{VV}}^{\text{max, dB}}$ must be calibrated for a given location. Imperfect calibration will result in estimation errors. In practice, the copolarized backscatter cross sections can be readily calibrated using known targets and techniques with considerable heritage. Hence, to simplify the analysis, we do not consider calibration errors in copolarized backscatter coefficients. We therefore consider the sensitivity of RVI to changes in σ_{HV} and the sensitivity of m_s to changes in $\sigma_{\text{VV}}^{\text{min, dB}}$ and $\sigma_{\text{VV}}^{\text{max, dB}}$.

RVI calibration uncertainty is dominated by uncertainty in the cross-polarized term. Let $\widehat{\sigma_{\text{HV}}} = a + b\sigma_{\text{HV}}$ (where all terms are in linear units) be the imperfectly calibrated cross-polarized backscatter coefficient. This error model accounts for mean and amplitude biases; more complex error models are beyond the scope of this study. We adopt the elasticity, a dimensionless measure of sensitivity, in this analysis. The elasticity of RVI with respect to b is defined as

$$\lim_{\Delta b \to 0} \frac{\frac{\Delta \text{RVI}}{\text{RVI}}}{\frac{\Delta b}{b}} = \frac{b}{\text{RVI}} \frac{\partial \text{RVI}}{\partial b}.$$

Assuming that the imperfectly calibrated value is locally "near" the calibrated value, we may evaluate the elasticity at $a = 0$, $b = 1$ to get

$$E_{\text{RVI},b}$$

$$= \frac{b}{\text{RVI}} \frac{\partial \text{RVI}}{\partial b} \Big|_{a=0,b=1}$$

$$= \left(\frac{\sigma_{\text{HV}}b}{a + b\sigma_{\text{HV}}} - \frac{2\sigma_{\text{HV}}b}{\sigma_{\text{HH}} + \sigma_{\text{VV}} + 2(a + b\sigma_{\text{HV}})} \right) \Big|_{a=0,b=1}$$

$$= 1 - \frac{\text{RVI}}{4}.$$

The elasticity of RVI with respect to a is undefined at $a = 0$. Instead, we consider the proportional error induced by nonzero a, i.e.,

$$\epsilon_a = \frac{\Delta \text{RVI}}{\text{RVI}} = \frac{\text{RVI} - \widehat{\text{RVI}}|_{b=1}}{\text{RVI}}$$

$$= 1 - \frac{(a + \sigma_{\text{HV}})(2\sigma_{\text{HV}} + \sigma_{\text{HH}} + \sigma_{\text{VV}})}{\sigma_{\text{HV}}(2a + 2\sigma_{\text{HV}} + \sigma_{\text{HH}} + \sigma_{\text{VV}})}$$

where $\widehat{\text{RVI}}|_{b=1}$ is calculated using $\widehat{\sigma_{\text{HV}}} = a + \sigma_{\text{HV}}$ instead of σ_{HV} in (1). If we fix a maximum allowed calibration error $|\epsilon_a|$ and rearrange for a, we obtain an upper bound on the calibration bias allowed to achieve the error requirement

$$|a| \leq a_{\max} = \frac{\sigma_{\text{HV}}|\epsilon_a|(2\sigma_{\text{HV}} + \sigma_{\text{HH}} + \sigma_{\text{VV}})}{2\sigma_{\text{HV}}|\epsilon_a| + \sigma_{\text{HH}} + \sigma_{\text{VV}}}.$$

It is convenient to express this maximum bias in decibels. In decibels, $a_{\max}$ is given by

$$a_{\max}^{\text{dB}} = -10 \log_{10}(\sigma_{\text{HV}}) - (-10 \log_{10}(\sigma_{\text{HV}} + a_{\max}))$$

$$= -10 \log_{10} \left(\frac{\sigma_{\text{HV}}}{\sigma_{\text{HV}} + a_{\max}} \right).$$

(6)

The m_s calibration error is determined by the $\sigma_{\text{VV}}^{\text{min, dB}}$ and $\sigma_{\text{VV}}^{\text{max, dB}}$ terms. The elasticity of m_s with respect to $\sigma_{\text{VV}}^{\text{min, dB}}$ is

$$E_{m_s, \sigma_{\text{VV}}^{\text{min, dB}}} = \frac{\sigma_{\text{VV}}^{\text{min, dB}}}{m_s} \frac{\partial m_s}{\partial \sigma_{\text{VV}}^{\text{min, dB}}}$$

$$= \frac{\sigma_{\text{VV}}^{\text{min, dB}}}{\sigma_{\text{VV}}^{\text{max, dB}} - \sigma_{\text{VV}}^{\text{min, dB}}} \frac{\sigma_{\text{VV}} - \sigma_{\text{VV}}^{\text{max, dB}}}{\sigma_{\text{VV}} - \sigma_{\text{VV}}^{\text{min, dB}}}$$

$$= \frac{\sigma_{\text{VV}}^{\text{min, dB}}}{\sigma_{\text{VV}}^{\text{max, dB}} - \sigma_{\text{VV}}^{\text{min, dB}}} \left(1 - \frac{1}{m_s} \right)$$

$$= -M \left(1 - \frac{1}{m_s} \right)$$

(7)

where

$$M = \frac{-\sigma_{\text{VV}}^{\text{min, dB}}}{\sigma_{\text{VV}}^{\text{max, dB}} - \sigma_{\text{VV}}^{\text{min, dB}}}.$$

The elasticity of m_s with respect to $\sigma_{\text{VV}}^{\text{max, dB}}$ is

$$E_{m_s, \sigma_{\text{VV}}^{\text{max, dB}}} = \frac{\sigma_{\text{VV}}^{\text{max, dB}}}{m_s} \frac{\partial m_s}{\partial \sigma_{\text{VV}}^{\text{max, dB}}} = \frac{-\sigma_{\text{VV}}^{\text{max, dB}}}{\sigma_{\text{VV}}^{\text{max, dB}} - \sigma_{\text{VV}}^{\text{min, dB}}}$$

$$= \frac{-\sigma_{\text{VV}}^{\text{min, dB}}}{\sigma_{\text{VV}}^{\text{max, dB}} - \sigma_{\text{VV}}^{\text{min, dB}}} - 1 = M - 1.$$

III. RESULTS AND DISCUSSION

A. Aquarius Observations

Global observations of (temporally averaged) mean RVI generally match known vegetation patterns, with some exceptions. Fig. 2 shows a global map of mean RVI, which is generated from Aquarius observations over the study period. In general, the RVI distinguishes between vegetation density well. It captures regions of dense vegetation, such as those in the Amazon and Congo, which have consistently high RVI. More sparsely vegetated regions in northern Russia and deciduous forests in the northern United States are also well represented, with lower mean RVI values. Regions with little vegetation are also generally well characterized, with low RVI values. However, there are clearly erroneous regions where vegetation is significantly overestimated, including the central Sahara and most of central Australia. Freezing soil is likely negatively biasing RVI in northern Russia.

Similarly, global observations of mean m_s generally match known soil moisture climatology, again, with some exceptions. Fig. 3 shows a global map of mean m_s, generated from the same Aquarius observations. Given the variability of soil moisture in time, it captures well the dominant soil wetness conditions
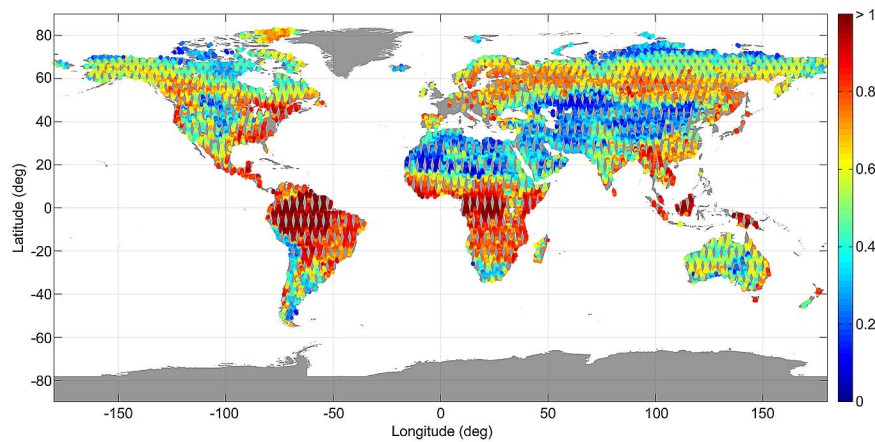
This article has been accepted for inclusion in a future issue of this journal. Content is final as presented, with the exception of pagination.

MCCOLL *et al.*: UNCERTAINTY ANALYSIS OF SOIL MOISTURE AND VEGETATION INDICES
5

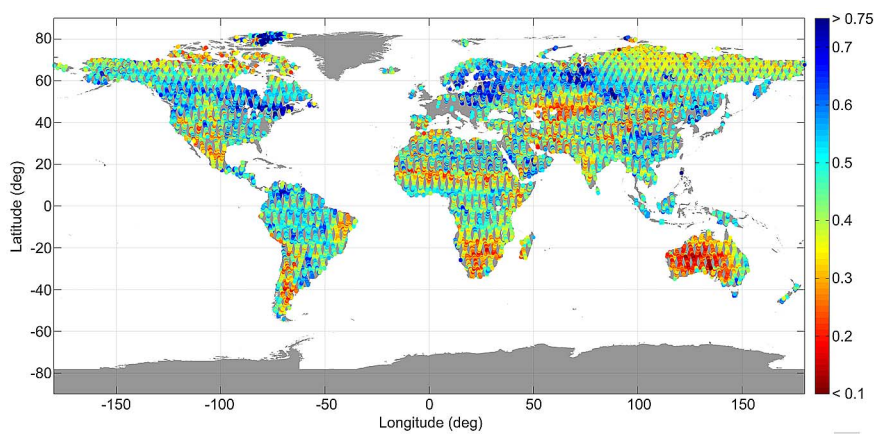Fig. 2. Mean observed RVI, calculated using one year of Aquarius observations in (1), starting September 1, 2011.

Fig. 3. Mean observed m_s, calculated using one year of Aquarius observations in (2), starting September 1, 2011.
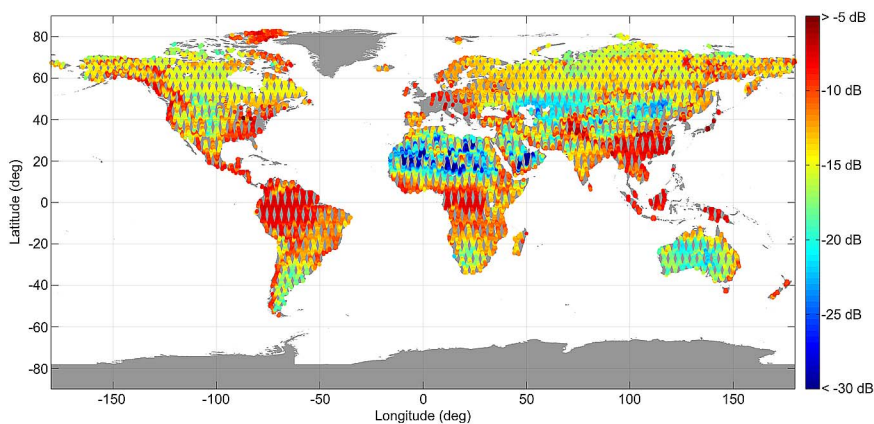
Fig. 4. Minimum observed σ_{VV} (in decibels) over one year of Aquarius observations, starting September 1, 2011.

around the world. The northern United States, Pampas region in South America, and boreal regions in northeastern Europe and western Russia display the highest mean soil wetness conditions. Central and western Australia, southern Africa, the Nordeste region in South America, and the southern reaches of the Sahara are among the driest regions. However, soil wetness conditions in most of the Sahara are clearly overestimated, as are those in much of the Taklamakan desert. In [17], these large deserts are masked out, as are the Amazon, Congo, and densely

vegetated regions in Indonesia and Malaysia. Furthermore, substantial empirical bias corrections (of up to 6 dB) are applied to $\sigma_{\max}^{0,\,dB}$ in the Arabian Peninsula, Northern Africa, southwestern United States, Chile and Patagonia, and central Asia.

While the minimum and maximum backscatter coefficients in a time series are highly sensitive to outliers, the minimum and maximum values in the Aquarius time series are reasonable and consistent with expectations. Fig. 4 shows a global map of minimum observed VV copolarized backscatters, in
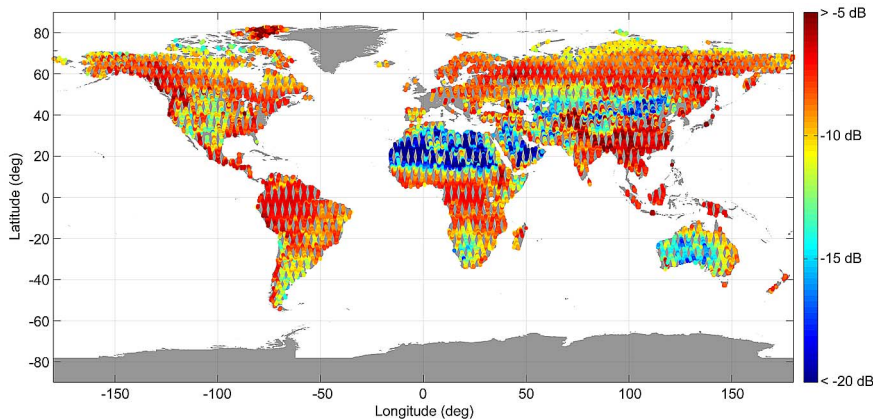
This article has been accepted for inclusion in a future issue of this journal. Content is final as presented, with the exception of pagination.

6   IEEE TRANSACTIONS ON GEOSCIENCE AND REMOTE SENSING

Fig. 5.   Maximum observed σ_{VV} (in decibels) over one year of Aquarius observations, starting September 1, 2011.
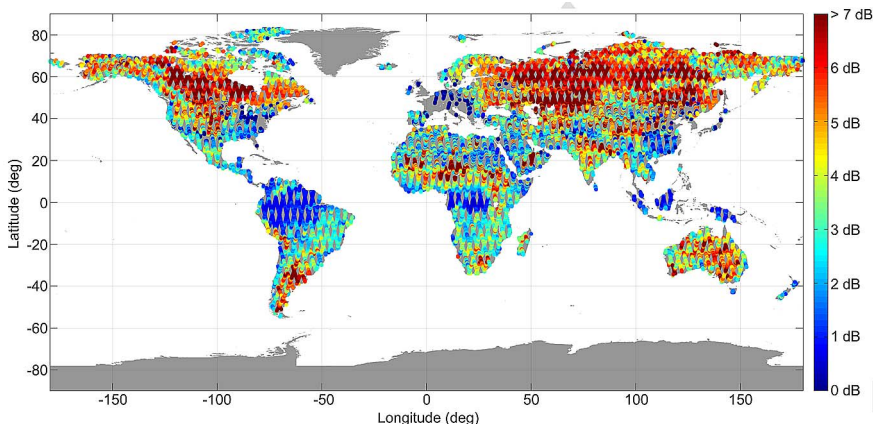

Fig. 6.   Dynamic range of σ_{VV} (in decibels) over one year of Aquarius observations, starting September 1, 2011.

decibels. In general, high copolarized backscatters may result from strong surface scattering, volume scattering, or double-bounce interactions between vegetation and the surface [9]. If the dominant scattering mechanism is surface scattering, backscatters will be higher when soils are wet rather than dry. A high minimum value indicates that the region is either consistently well vegetated or the soil is consistently wet. The Aquarius data show that high minimum values of σ_{VV} coincide with well-vegetated regions in the Amazon, Congo, southeast Asia, and the United States. The lowest minimum values occur in dry nonvegetated regions such as the Sahara, Arabian Peninsula, central Australia, Kazakhstan, and Mongolia. Fig. 5 shows a global map of maximum observed VV copolarized backscatters, in decibels. A low maximum value indicates that the region is either consistently lightly vegetated or the soil is consistently dry. As expected, the lowest maximum values coincide with deserts.

The observed dynamic range is low in both consistently well-vegetated wet regions (such as the Amazon) and lightly vegetated dry regions (such as the Sahara). Fig. 6 shows the dynamic range of σ_{VV}, in decibels. It is highest in the northern hemisphere over regions where there is a strong seasonal change in soil moisture and vegetation (such as the northern United States and Canada). The Pampas region in South America—where irrigation leads to strong variability in moisture and vegetation—and transition regions between

deserts and forests (e.g., the Sahel) also exhibit a high dynamic range. Complex spatial patterns of high dynamic range regions over Australia are likely the result of combinations of irrigation (in southwestern Australia and the Murray–Darling Basin) and above-average precipitation leading to flooding in the otherwise arid inland regions. The very low dynamic ranges observed over Europe and the eastern United States are likely a product of estimation errors resulting from only using one year of data. On the whole, the global map is very similar to that of a previous study [5, Fig. 11(b)]. The main differences occur in regions where the dynamic range is very small; however, in [5], a bias correction factor of up to 5 dB is applied to regions where the soil is likely never saturated. Given that this map was produced using observations from a different satellite, over a different time period, and using a different method, the similarity suggests that the estimates obtained are reasonable, despite being obtained from only one year of observations. Furthermore, the dynamic range of σ_{HH} (see Fig. 7) is almost identical to that of σ_{VV}, with only minor differences between the two.

B. Target Region Observations

A select number of target regions are defined in order to focus on the temporal behavior of the indices at a site, in addition to the global analysis with the complete Aquarius ice-free land
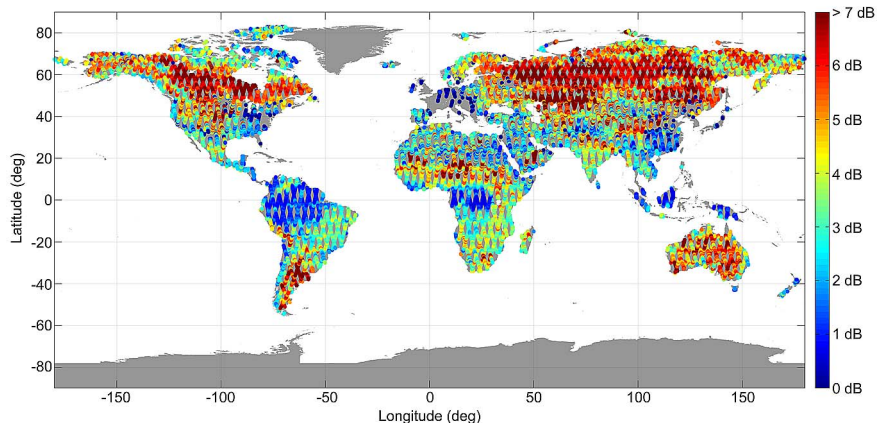
Fig. 7. Dynamic range of σ_{HH} (in decibels) over one year of Aquarius observations, starting September 1, 2011.

coverage. RVI and m_s display distinct seasonal cycles and responses to precipitation. Fig. 8 compares time series of RVI, m_s, and precipitation at eight target regions around the world. The source of the precipitation data is the $0.25°$ three-hourly CMORPH precipitation product [20]. Aquarius observations were averaged to weekly values and used to calculate weekly RVI and m_s values. In each target region, the median RVI and m_s are plotted. It can be seen that, in many cases, m_s and RVI are able to distinguish between changes in soil moisture and vegetation. For instance, while the time series are noisy, m_s is immediately responsive to March precipitation events in the Murrumbidgee region, whereas RVI is not. Similar behavior occurs in the Pampas region during February and March. Over the Amazon and Tanzania, a clear seasonal cycle is evident in m_s that is not present in RVI. The dynamic range of RVI is smaller than that of m_s for most target areas since it does not use a region-specific calibration. RVI is most variable in the Murrumbidgee and SMAPVEX12 target areas. Both these regions are dominated by irrigated agriculture, with variability in crop types and phenology likely contributing to the noisiness in the time series. m_s is significantly positively biased over the Sahara. We consider a potential reason for this bias later in this paper.

C. Noise Error Analysis

Estimation errors in RVI due to noise are positively correlated with RVI. Fig. 9 shows the noise-induced standard error in estimates of RVI. In general, it is positively correlated with vegetation and RVI and can be substantial. The bias in RVI due to noise is very low across all vegetation conditions (not shown). These results suggest that RVI estimates will require considerable averaging (with multiple looks or temporal averaging) to overcome estimation errors from propagated noise. Fortunately, the low bias means that these errors can be averaged out with no residual bias.

Estimates of m_s are usually highly sensitive to errors when the dynamic range is low. Fig. 10 shows how the absolute bias and standard error of m_s estimates vary with dynamic range in the presence of noise. Where the dynamic range is small (< 1 dB), both the bias and the standard error in m_s are very large. Due to the spatial and temporal averaging of m_s

in Figs. 3 and 8, its high standard error is not apparent. In general, however, regions in which the σ_{VV} dynamic range is small will require significant averaging to remove estimation errors. Even with sufficient averaging, biases will remain that cannot be removed.

Estimation errors in m_s are highest over highly vegetated and very dry regions and agree well with previous studies. Fig. 11 shows the bias induced in estimates of m_s by noise. The bias is consistently very low everywhere, except for highly vegetated regions like the Amazon and Congo. Fig. 12 shows the standard error in estimates of m_s due to noise. It is highest over highly vegetated (e.g., Amazon and Congo) and very dry regions (e.g., Sahara and Arabian Peninsula). These results are also in agreement with those of a previous study [5, Fig. 11(c)]. The order of magnitude of errors is consistent, noting that we display the standard error, whereas the variance is mapped in [5]. Furthermore, bias corrections made in [5] over some regions where the dynamic range is low will result in lower m_s standard error estimates in that study. There is some disagreement over the eastern United States and southeastern China; these discrepancies over populated areas may be due to unflagged RFI in the Aquarius observations.

D. Calibration Error Analysis

RVI is sensitive to additive errors, such as those from uncertain calibration, in the cross-polarized backscatter coefficient. Fig. 13 shows the maximum cross-polarized calibration bias a_{max}^{dB} allowed to maintain calibration error in the range $|\epsilon_a| \leq 0.1$, for different combinations of mean σ_{HV} and $\sigma_{HH} + \sigma_{VV}$ observed by Aquarius during the study period. While the tolerated bias is small in all cases, it is higher for higher backscatter values since the bias makes a smaller contribution relative to the overall signal. As the backscatter values decrease, the tolerated bias rapidly decreases. Since the cross-polarized backscatter coefficient appears in both the numerator and the denominator of RVI, the calibration bias will positively bias RVI for sufficiently small backscatters, regardless of the sign of a. Note that some of the Aquarius observed values are below the SMAP noise floor (conservatively, -28 dB for copolarized and -25 dB for cross-polarized). Fig. 14 plots a_{max}^{dB} for $|\epsilon_a| \leq 0.1$ globally using mean backscatter observations from Aquarius.

This article has been accepted for inclusion in a future issue of this journal. Content is final as presented, with the exception of pagination.

8   IEEE TRANSACTIONS ON GEOSCIENCE AND REMOTE SENSING
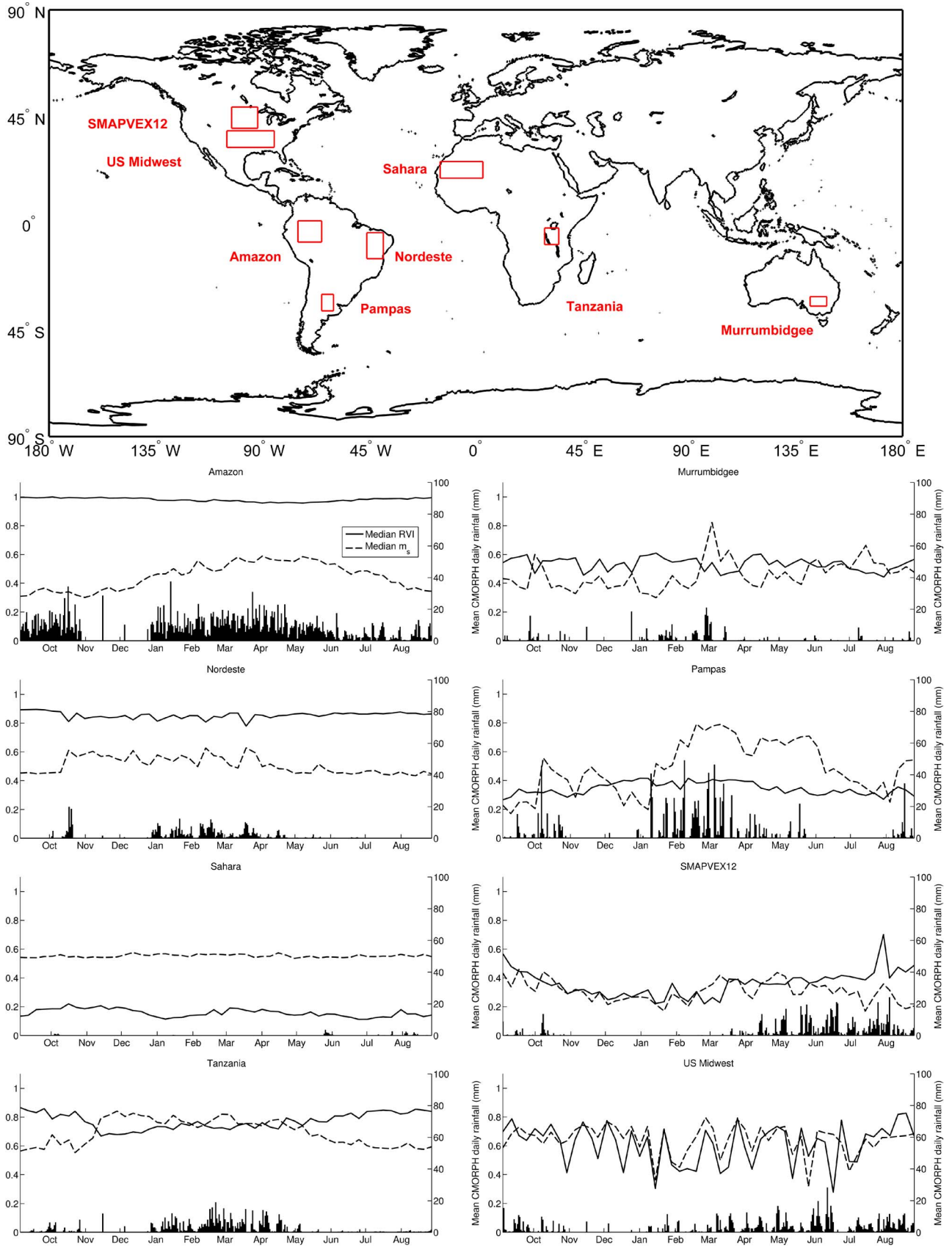

Fig. 8. Time series of median RVI, median m_s, and mean precipitation over eight target areas. RVI and m_s values are calculated at weekly intervals; precipitation is calculated daily.
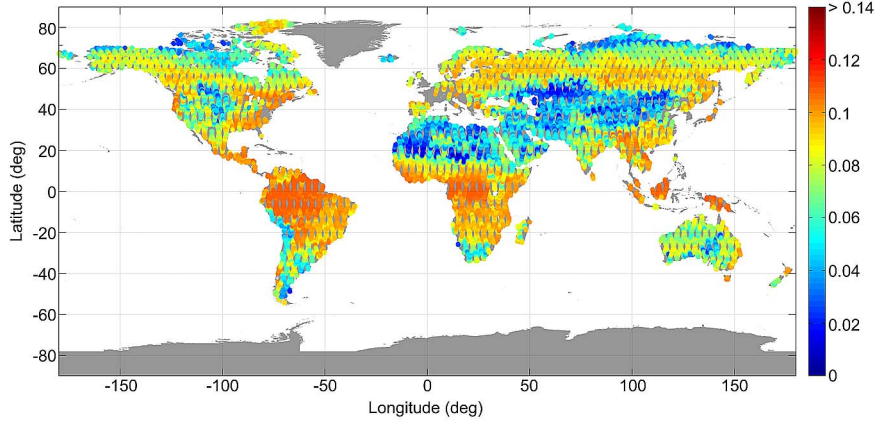
Fig. 9. Global map of RVI standard error, using $K_{p_{pp}} = K_{p_{pq}} = 0.18$ and mean backscatter in (3).
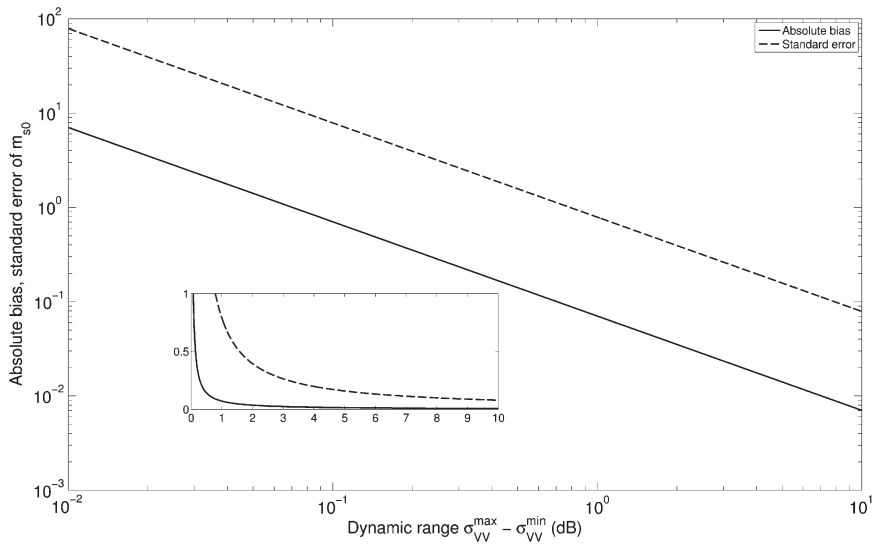

Fig. 10. Dynamic range dependence of the absolute bias [calculated using (4)] and standard error [calculated using (5)] in estimates of m_s in the presence of noise, for $K_p = 0.18$. The inset figure has the same axis labels.
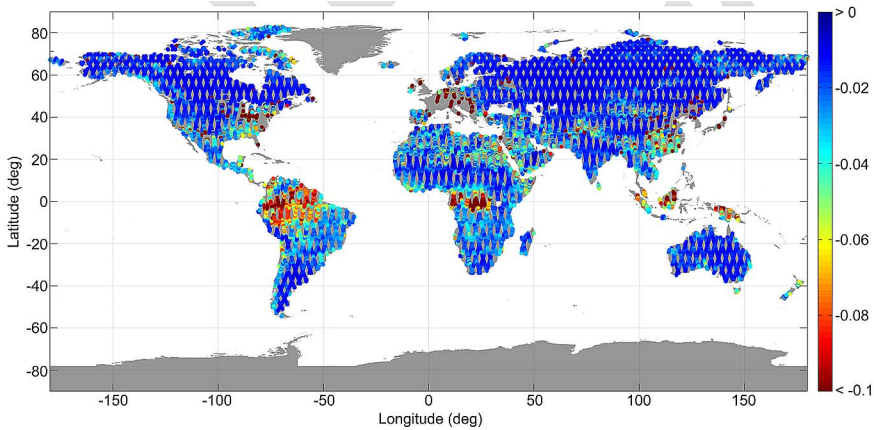

Fig. 11. Global map of bias in m_s, using $K_{p_{pp}} = K_{p_{pq}} = 0.18$ and (4).

Sensitivity of RVI to bias in the cross-polarized calibration offset is greatest in regions that are sparsely vegetated. In these regions, an offset as small as $a \sim 10^{-4}$ (in linear units) will result in RVI errors of 0.1.

In highly vegetated regions, which are of arguably greater interest in studies using RVI, the problem is significantly re-duced. RVI is relatively insensitive to the multiplicative term in the calibration error b. Near $(a, b) = (0, 1)$, $\Delta\text{RVI} = \Delta b \times \text{RVI} \times (1 - (\text{RVI}/4))$, which is, at most, $0.75\Delta b$. Therefore, we may expect strong positive biases in RVI in lightly vegetated regions (where σ_{HV} is very low) due to the cross-polarized cal-ibration bias, but multiplicative calibration errors are unlikely

This article has been accepted for inclusion in a future issue of this journal. Content is final as presented, with the exception of pagination.

10

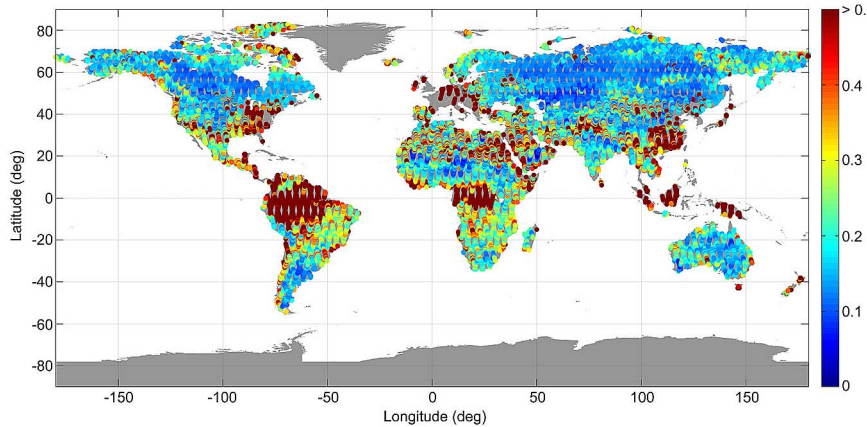IEEE TRANSACTIONS ON GEOSCIENCE AND REMOTE SENSING

Fig. 12. Global map of m_s standard error, using $K_{p_{pp}} = K_{p_{pq}} = 0.18$ and (5).
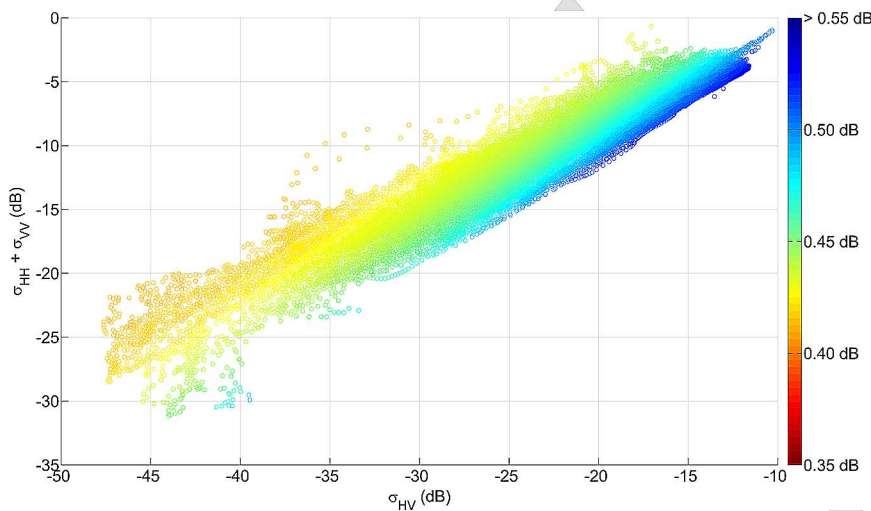

Fig. 13. Maximum cross-polarized calibration bias $a_{\max}^{\mathrm{dB}}$ allowed to maintain RVI calibration error in the range $|\epsilon_a| \leq 0.1$, plotted for combinations of mean σ_{HV} and total power $\sigma_{\mathrm{HH}} + \sigma_{\mathrm{VV}}$ observed by Aquarius during the study period. Total power is calculated in linear units and then converted to decibels. The values of a are calculated using (6).
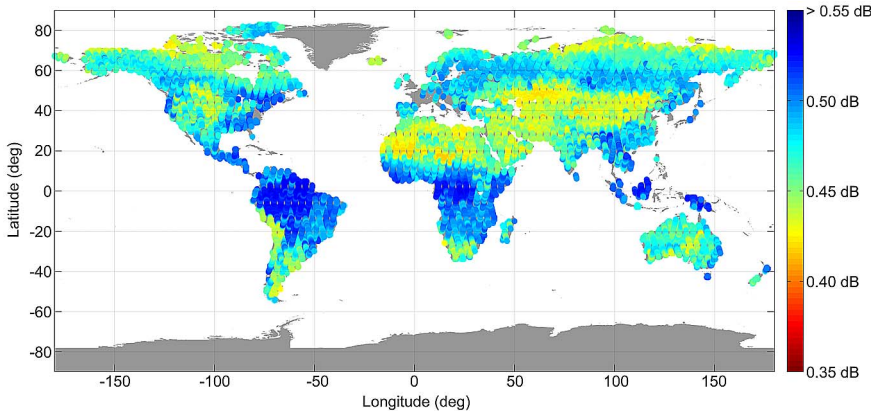

Fig. 14. Global map of $a_{\max}^{\mathrm{dB}}$ for $|\epsilon_a| \leq 0.1$.

to significantly affect results. This calibration error bias may be one explanation for the positive bias in RVI estimates over the Sahara and central Australia in Fig. 2.

While the calibration parameters in m_s correspond to physical quantities, there is still considerable uncertainty in their true value. For instance, due to outliers and noise, estimating

the true value of $\sigma_{\mathrm{VV}}^{\min,\,\mathrm{dB}}$ and $\sigma_{\mathrm{VV}}^{\max,\,\mathrm{dB}}$ is rarely as simple as taking the maximum and minimum values in a long time series. Fig. 15 shows the elasticity $E_{m_s, \sigma_{\mathrm{VV}}^{\min,\,\mathrm{dB}}}$ of m_s to $\sigma_{\mathrm{VV}}^{\min,\,\mathrm{dB}}$ for different combinations of m_s and M observed by Aquarius. For a given M, increasing m_s decreases the sensitivity of m_s to $\sigma_{\mathrm{VV}}^{\min,\,\mathrm{dB}}$. Fig. 16 plots M globally, using Aquarius
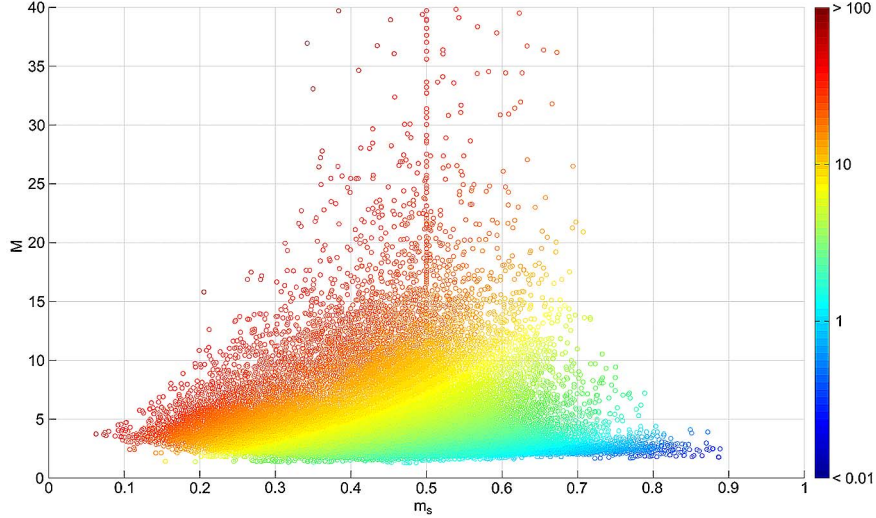
This article has been accepted for inclusion in a future issue of this journal. Content is final as presented, with the exception of pagination.

MCCOLL *et al.*: UNCERTAINTY ANALYSIS OF SOIL MOISTURE AND VEGETATION INDICES 11

Fig. 15. Elasticity of m_s with respect to $\sigma_{\mathrm{VV}}^{\mathrm{min, \, dB}}$ ($E_{m_s, \sigma_{\mathrm{VV}}^{\mathrm{min, \, dB}}}$) for values of m_s and M observed by Aquarius, calculated using (7). Aquarius observations with $M > 40$ are not shown for clarity.
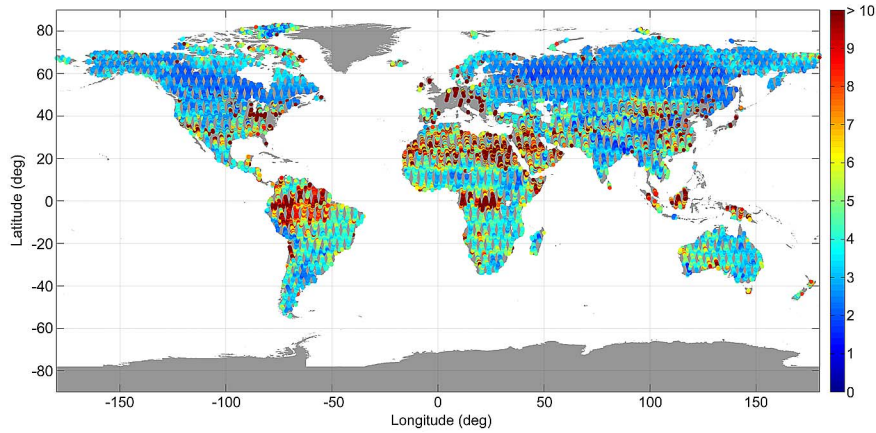

Fig. 16. Global map of M.

observations. It generally increases with decreasing dynamic range and is highest over the Amazon, Sahara, Congo, Arabian Peninsula, and Europe. Increasing M leads to substantially greater sensitivity to both $\sigma_{\mathrm{VV}}^{\mathrm{min, \, dB}}$ and $\sigma_{\mathrm{VV}}^{\mathrm{max, \, dB}}$. These results show that $E_{m_s, \sigma_{\mathrm{VV}}^{\mathrm{min, \, dB}}}$ and $E_{m_s, \sigma_{\mathrm{VV}}^{\mathrm{max, \, dB}}}$ are considerable wherever the dynamic range is small, over deserts, densely vegetated regions, or regions with complex topography. Potential methods to mitigate this sensitivity include removing outliers or setting maximum and minimum backscatter values to averages of ranges of extreme high and low values, respectively. Regions where the soil either never saturates (e.g., deserts) or never completely dries (e.g., rainforests) will require empirical bias corrections, such as those described in [5] or [6] and used in [17].

It should be noted that this study considers noise errors and calibration errors independently, as in previous studies [5], [6]. However, errors may interact nonlinearly. These impacts require further investigation. We also do not consider errors that cannot be represented in a K_p noise framework, which likely include some errors due to terrain inhomogeneity, an error source, which warrants further attention. Finally, an alternative explanation for the relatively high backscatters observed over deserts is that the results are not due to measurement errors

but to real soil volume scattering. For dry soils, the penetration depth at L-band may extend to a meter or more, leading to non-negligible volume scattering [21], [22]. There are insufficient data to test this hypothesis, but it deserves attention in future studies.

IV. CONCLUSION

This study has quantified the likely impacts of SMAP radar backscatter cross-section uncertainty on satellite estimates of two radar-only vegetation and soil moisture indices: RVI and m_s. We use new observations from the Aquarius satellite mission to map these impacts globally. The regional patterns of the Aquarius observations (in particular, the dynamic range of σ_{VV}) are consistent with expectations and previous studies. Over a range of different landcover conditions, RVI and m_s exhibit distinct seasonal cycles and responses to precipitation. However, while the RVI generally captures vegetation patterns well, it significantly overestimates biomass in some dry regions. We suggest that this may be due to the high sensitivity of RVI to additive calibration errors in the cross-polarized backscatter coefficient over lightly vegetated regions. Estimation errors in

RVI due to noise are positively correlated with RVI and can be large. However, since there is no significant mean bias, sufficient temporal/spatial averaging can remove these errors. Similarly, m_s tends to overestimate soil wetness in particularly dry regions. This is primarily due to the low dynamic range in σ_{VV} exhibited over these regions. Noise induces significant bias and variance in m_s estimates in regions where the dynamic range is small (e.g., dense forests and deserts). In addition, m_s is particularly sensitive to calibration errors in regions where the dynamic range is small. Based on these findings, we recommend that global m_s retrievals should be masked in regions where the dynamic range is small, such as over dense forest and deserts. Global RVI observations should be masked over lightly vegetated regions. Elsewhere, RVI should be calculated using backscatter coefficients averaged over a sufficiently large spatial or temporal window to reduce the effects of noise. These restrictions are relatively minor since soil moisture retrievals are usually masked over deserts and forests and RVI is of main interest over vegetated regions. We find that these indices may be estimated by satellites with sufficient precision over areas of greatest interest to be used by the SMAP science and application community, provided they are carefully applied.

APPENDIX A
DERIVATION OF RVI NOISE UNCERTAINTY

RVI is defined as

$$\mathrm{RVI} = \frac{8\sigma_{\mathrm{HV}}}{\sigma_{\mathrm{HH}}+\sigma_{\mathrm{VV}}+2\sigma_{\mathrm{HV}}} = f\left([\sigma_{\mathrm{HH}},\sigma_{\mathrm{VV}},\sigma_{\mathrm{HV}}]^T\right) = f(\boldsymbol{\sigma}).$$

The observed RVI is $\mathrm{RVI}_0 = f\left([\sigma_{\mathrm{HH}_0},\sigma_{\mathrm{VV}_0},\sigma_{\mathrm{HV}_0}]^T\right) = f(\boldsymbol{\sigma}_0)$. In order to understand the impact of noise on RVI estimation, we Taylor expand RVI_0 to about the true backscatter values $\boldsymbol{\sigma}$, retaining up to second-order terms, to obtain

$$\mathrm{RVI}_0 \approx f(\boldsymbol{\sigma}) + \boldsymbol{J}(\boldsymbol{\sigma})(\boldsymbol{\sigma_0}-\boldsymbol{\sigma}) + \frac{1}{2}(\boldsymbol{\sigma_0}-\boldsymbol{\sigma})^T\boldsymbol{H}(\boldsymbol{\sigma})(\boldsymbol{\sigma_0}-\boldsymbol{\sigma})$$

where

$$\boldsymbol{J}(\boldsymbol{\sigma}) = \left[\begin{array}{ccc} \left.\frac{\partial f(\boldsymbol{\sigma_0})}{\partial\sigma_{\mathrm{HH}_0}}\right|_{\boldsymbol{\sigma}} & \left.\frac{\partial f(\boldsymbol{\sigma_0})}{\partial\sigma_{\mathrm{VV}_0}}\right|_{\boldsymbol{\sigma}} & \left.\frac{\partial f(\boldsymbol{\sigma_0})}{\partial\sigma_{\mathrm{HV}_0}}\right|_{\boldsymbol{\sigma}} \end{array}\right]$$

$$= \left[\begin{array}{ccc} \frac{-\mathrm{RVI}^2}{8\sigma_{\mathrm{HV}}} & \frac{-\mathrm{RVI}^2}{8\sigma_{\mathrm{HV}}} & \left(\frac{\mathrm{RVI}}{\sigma_{\mathrm{HV}}}-\frac{\mathrm{RVI}^2}{4\sigma_{\mathrm{HV}}}\right) \end{array}\right]$$

is the Jacobian matrix,

$$\boldsymbol{H}(\boldsymbol{\sigma}) = \begin{bmatrix} \left.\frac{\partial^2 f(\boldsymbol{\sigma_0})}{\partial\sigma_{\mathrm{HH}_0}^2}\right|_{\boldsymbol{\sigma}} & \left.\frac{\partial^2 f(\boldsymbol{\sigma_0})}{\partial\sigma_{\mathrm{HH}_0}\partial\sigma_{\mathrm{VV}_0}}\right|_{\boldsymbol{\sigma}} & \left.\frac{\partial^2 f(\boldsymbol{\sigma_0})}{\partial\sigma_{\mathrm{HH}_0}\partial\sigma_{\mathrm{HV}_0}}\right|_{\boldsymbol{\sigma}} \\[2mm] \left.\frac{\partial^2 f(\boldsymbol{\sigma_0})}{\partial\sigma_{\mathrm{VV}_0}\partial\sigma_{\mathrm{HH}_0}}\right|_{\boldsymbol{\sigma}} & \left.\frac{\partial^2 f(\boldsymbol{\sigma_0})}{\partial\sigma_{\mathrm{VV}_0}^2}\right|_{\boldsymbol{\sigma}} & \left.\frac{\partial^2 f(\boldsymbol{\sigma_0})}{\partial\sigma_{\mathrm{VV}_0}\partial\sigma_{\mathrm{HV}_0}}\right|_{\boldsymbol{\sigma}} \\[2mm] \left.\frac{\partial^2 f(\boldsymbol{\sigma_0})}{\partial\sigma_{\mathrm{HV}_0}\partial\sigma_{\mathrm{HH}_0}}\right|_{\boldsymbol{\sigma}} & \left.\frac{\partial^2 f(\boldsymbol{\sigma_0})}{\partial\sigma_{\mathrm{HV}_0}\partial\sigma_{\mathrm{VV}_0}}\right|_{\boldsymbol{\sigma}} & \left.\frac{\partial^2 f(\boldsymbol{\sigma_0})}{\partial\sigma_{\mathrm{HV}_0}^2}\right|_{\boldsymbol{\sigma}} \end{bmatrix}$$

$$= \begin{bmatrix} \frac{\mathrm{RVI}^3}{32\sigma_{\mathrm{HV}}^2} & \frac{\mathrm{RVI}^3}{32\sigma_{\mathrm{HV}}^2} & \left(\frac{\mathrm{RVI}^3}{16\sigma_{\mathrm{HV}}^2}-\frac{\mathrm{RVI}}{\sigma_{\mathrm{HV}}}\right) \\[2mm] \frac{\mathrm{RVI}^3}{32\sigma_{\mathrm{HV}}^2} & \frac{\mathrm{RVI}^3}{32\sigma_{\mathrm{HV}}^2} & \left(\frac{\mathrm{RVI}^3}{16\sigma_{\mathrm{HV}}^2}-\frac{\mathrm{RVI}}{\sigma_{\mathrm{HV}}}\right) \\[2mm] \left(\frac{\mathrm{RVI}^3}{16\sigma_{\mathrm{HV}}^2}-\frac{\mathrm{RVI}}{\sigma_{\mathrm{HV}}}\right) & \left(\frac{\mathrm{RVI}^3}{16\sigma_{\mathrm{HV}}^2}-\frac{\mathrm{RVI}}{\sigma_{\mathrm{HV}}}\right) & \left(\frac{\mathrm{RVI}^3}{8\sigma_{\mathrm{HV}}^2}-\frac{\mathrm{RVI}^2}{2\sigma_{\mathrm{HV}}^2}\right) \end{bmatrix}$$

is the Hessian matrix and

$$\boldsymbol{\sigma_0}-\boldsymbol{\sigma} = \left[\begin{array}{ccc} K_{p_{pp}}\sigma_{\mathrm{HH}}\omega & K_{p_{pp}}\sigma_{\mathrm{VV}}\omega & K_{p_{pq}}\sigma_{\mathrm{HV}}\omega \end{array}\right]^T.$$

We can now estimate the first two moments of RVI_0 using its Taylor expansion. Since $E(\omega) = 0$ and $E(\omega^2) = 1$, and by linearity of the expectation operator, we have

$$E(\mathrm{RVI}_0) \approx \mathrm{RVI} + \frac{K_{p_{pp}}^2\mathrm{RVI}^3}{64\sigma_{\mathrm{HV}}^2}(\sigma_{\mathrm{HH}}+\sigma_{\mathrm{VV}})^2$$
$$+ \frac{K_{p_{pq}}^2\mathrm{RVI}^2}{4}\left(\frac{\mathrm{RVI}}{4}-1\right) + \frac{K_{pc_{pp}}K_{pc_{pq}}\mathrm{RVI}^2}{8\sigma_{\mathrm{HV}}}$$
$$\times \left(\frac{\mathrm{RVI}}{2}-1\right)(\sigma_{\mathrm{HH}}+\sigma_{\mathrm{VV}}).$$

The variance can be also estimated from the Taylor series. Proceeding term by term, as for the expected value derivation, and using the identities $\mathrm{Var}(aX+b) = a^2\mathrm{Var}(X)$, $\mathrm{Var}(\omega) = 1$, $\mathrm{Var}(\omega^2) = 2$, and $\mathrm{Var}(\omega_i\omega_j) = 0$ for $i \neq j$, we obtain

$$\mathrm{Var}(\mathrm{RVI}_0)$$
$$\approx \left(K_{pc_{pq}}\mathrm{RVI}\left(1-\frac{\mathrm{RVI}}{4}\right)-\frac{K_{pc_{pp}}\mathrm{RVI}^2}{8\sigma_{\mathrm{HV}}}(\sigma_{\mathrm{HH}}+\sigma_{\mathrm{VV}})\right)^2$$
$$+ 2\left(\frac{K_{p_{pp}}^2\mathrm{RVI}^3}{64\sigma_{\mathrm{HV}}^2}(\sigma_{\mathrm{HH}}+\sigma_{\mathrm{VV}})^2\right.$$
$$+ \frac{K_{pc_{pp}}K_{pc_{pq}}\mathrm{RVI}^2}{8\sigma_{\mathrm{HV}}}\left(\frac{\mathrm{RVI}}{2}-1\right)(\sigma_{\mathrm{HH}}+\sigma_{\mathrm{VV}})$$
$$\left.+ \frac{K_{p_{pq}}^2\mathrm{RVI}^2}{4}\left(\frac{\mathrm{RVI}}{4}-1\right)\right)^2.$$

APPENDIX B
DERIVATION OF m_s NOISE UNCERTAINTY

m_s is a function of σ_{VV} defined as

$$m_s(\sigma_{\mathrm{VV}}) = \frac{10\log_{10}(\sigma_{\mathrm{VV}})-\sigma_{\mathrm{VV}}^{\mathrm{min,\ dB}}}{\sigma_{\mathrm{VV}}^{\mathrm{max,\ dB}}-\sigma_{\mathrm{VV}}^{\mathrm{min,\ dB}}} = g(\sigma_{\mathrm{VV}}).$$

The observed m_s is given by

$$m_{s_0} = g(\sigma_{\mathrm{VV}_0}) = \frac{10\log_{10}(\sigma_{\mathrm{VV}_0})-\sigma_{\mathrm{VV}}^{\mathrm{min,\ dB}}}{\sigma_{\mathrm{VV}}^{\mathrm{max,\ dB}}-\sigma_{\mathrm{VV}}^{\mathrm{min,\ dB}}}$$
$$= \frac{10\log_{10}(\sigma_{\mathrm{VV}})+10\log_{10}(1+K_p\omega)-\sigma_{\mathrm{VV}}^{\mathrm{min,\ dB}}}{\sigma_{\mathrm{VV}}^{\mathrm{max,\ dB}}-\sigma_{\mathrm{VV}}^{\mathrm{min,\ dB}}}.$$

We Taylor expand m_{s_0} to about the true backscatter value σ_{VV}, retaining up to second-order terms, to get

$$m_{s_0} \approx g(\sigma_{\mathrm{VV}}) + \left.\frac{\partial g}{\partial\sigma_{\mathrm{VV}_0}}\right|_{\sigma_{\mathrm{VV}}}(\sigma_{\mathrm{VV}_0}-\sigma_{\mathrm{VV}})$$
$$+ \frac{1}{2}\left.\frac{\partial^2 g}{\partial\sigma_{\mathrm{VV}_0}^2}\right|_{\sigma_{\mathrm{VV}}}(\sigma_{\mathrm{VV}_0}-\sigma_{\mathrm{VV}})^2$$
$$= g(\sigma_{\mathrm{VV}}) + \left.\frac{\partial g}{\partial\sigma_{\mathrm{VV}_0}}\right|_{\sigma_{\mathrm{VV}}}(K_p\omega\sigma_{\mathrm{VV}})$$
$$+ \frac{1}{2}\left.\frac{\partial^2 g}{\partial\sigma_{\mathrm{VV}_0}^2}\right|_{\sigma_{\mathrm{VV}}}(K_p\omega\sigma_{\mathrm{VV}})^2.$$

This article has been accepted for inclusion in a future issue of this journal. Content is final as presented, with the exception of pagination.

MCCOLL *et al.*: UNCERTAINTY ANALYSIS OF SOIL MOISTURE AND VEGETATION INDICES
13

The derivatives of g are

$$\frac{\partial g}{\partial \sigma_{\mathrm{VV}_0}}\bigg|_{\sigma_{\mathrm{VV}}} = \frac{10}{\ln(10)\left(\sigma_{\mathrm{VV}}^{\mathrm{max,\ dB}} - \sigma_{\mathrm{VV}}^{\mathrm{min,\ dB}}\right)}\frac{1}{\sigma_{\mathrm{VV}}}$$

$$\frac{\partial^2 g}{\partial \sigma_{\mathrm{VV}_0}^2}\bigg|_{\sigma_{\mathrm{VV}}} = \frac{-10}{\ln(10)\left(\sigma_{\mathrm{VV}}^{\mathrm{max,\ dB}} - \sigma_{\mathrm{VV}}^{\mathrm{min,\ dB}}\right)}\frac{1}{\sigma_{\mathrm{VV}}^2}.$$

Therefore

$$m_{s_0} \approx g(\sigma_{\mathrm{VV}}) + \frac{10}{\ln(10)\left(\sigma_{\mathrm{VV}}^{\mathrm{max,\ dB}} - \sigma_{\mathrm{VV}}^{\mathrm{min,\ dB}}\right)}\left(K_p\omega - \frac{K_p^2\omega^2}{2}\right).$$

Using this expression to calculate the first two moments of m_{s_0}, we find

$$E(m_{s_0}) \approx m_s - \frac{5K_{pc}^2}{\ln(10)\left(\sigma_{\mathrm{VV}}^{\mathrm{max,\ dB}} - \sigma_{\mathrm{VV}}^{\mathrm{min,\ dB}}\right)}$$

$$\mathrm{Var}(m_{s_0}) \approx \left(\frac{10}{\ln(10)\left(\sigma_{\mathrm{VV}}^{\mathrm{max,\ dB}} - \sigma_{\mathrm{VV}}^{\mathrm{min,\ dB}}\right)}\right)^2\left(K_p^2 + \frac{K_p^4}{2}\right).$$

ACKNOWLEDGMENT

REFERENCES

[1] D. Entekhabi, E. Njoku, P. O'Neill, K. Kellogg, W. Crow, W. Edelstein, J. Entin, S. Goodman, T. Jackson, J. Johnson, J. Kimball, J. Piepmeier, R. Koster, N. Martin, K. McDonald, M. Moghaddam, S. Moran, R. Reichle, J. Shi, M. Spencer, S. Thurman, L. Tsang, and J. van Zyl, "The Soil Moisture Active Passive (SMAP) mission," *Proc. IEEE*, vol. 98, no. 5, pp. 704–716, May 2010.

[2] M. Arii, J. van Zyl, and Y. Kim, "A general characterization for polarimetric scattering from vegetation canopies," *IEEE Trans. Geosci. Remote Sens.*, vol. 48, no. 9, pp. 3349–3357, Sep. 2010.

[3] W. Wagner, G. Lemoine, M. Borgeaud, and H. Rott, "A study of vegetation cover effects on ERS scatterometer data," *IEEE Trans. Geosci. Remote Sens.*, vol. 37, no. 2, pp. 938–948, Mar. 1999.

[4] S. Kim, J. van Zyl, S. Dunbar, E. Njoku, J. Johnson, M. Moghaddam, J. Shi, and L. Tsang, "Algorithm Theoretical Basis Document (ATBD): SMAP L2 & L3 radar soil moisture (active) data products," Jet Propulsion Lab., Calif. Inst. Technol., Pasadena, CA, USA, Tech. Rep. Initial Release, v. 1, 2012.

[5] V. Naeimi, K. Scipal, Z. Bartalis, S. Hasenauer, and W. Wagner, "An improved soil moisture retrieval algorithm for ERS and METOP scatterometer observations," *IEEE Trans. Geosci. Remote Sens.*, vol. 47, no. 7, pp. 1999–2013, Jul. 2009.

[6] C. Pathe, W. Wagner, D. Sabel, M. Doubkova, and J. Basara, "Using ENVISAT ASAR global mode data for surface soil moisture retrieval over Oklahoma, USA," *IEEE Trans. Geosci. Remote Sens.*, vol. 47, no. 2, pp. 468–480, Feb. 2009.

[7] D. Le Vine, G. Lagerloef, F. Colomb, S. Yueh, and F. Pellerano, "Aquarius: An instrument to monitor sea surface salinity from space," *IEEE Trans. Geosci. Remote Sens.*, vol. 45, no. 7, pp. 2040–2050, Jul. 2007.

[8] Y. Kim and J. van Zyl, "On the relationship between polarimetric parameters," in *Proc. IEEE IGARSS Conf.*, 2000, pp. 1298–1300.

[9] A. Freeman and S. Durden, "A three-component scattering model for polarimetric SAR data," *IEEE Trans. Geosci. Remote Sens.*, vol. 36, no. 3, pp. 963–973, May 1998.

[10] M. Burgin, D. Clewley, R. Lucas, and M. Moghaddam, "A generalized radar backscattering model based on wave theory for multilayer multispecies vegetation," *IEEE Trans. Geosci. Remote Sens.*, vol. 49, no. 12, pp. 4832–4845, Dec. 2011.

[11] K. Rodriguez, J. Weissel, and Y. Kim, "Classification of landslide surfaces using fully polarimetric SAR: Examples from Taiwan," in *Proc. IEEE IGARSS Conf.*, 2002, pp. 2918–2920.

[12] J. Weissel, K. Czuchlewski, and Y. Kim, "Synthetic aperture radar (SAR)-based mapping of volcanic flows: Manam Island, Papua New Guinea," *Nat. Hazards Earth Syst. Sci.*, vol. 4, pp. 339–346, 2004.

[13] Y. Kim and J. van Zyl, "Vegetation effects on soil moisture estimation," in *Proc. IEEE IGARSS Conf.*, 2004, pp. 800–802.

[14] Y. Kim and J. van Zyl, "A time-series approach to estimate soil moisture using polarimetric radar data," *IEEE Trans. Geosci. Remote Sens.*, vol. 47, no. 8, pp. 2519–2527, Aug. 2009.

[15] W. Wagner, G. Lemoine, and H. Rott, "A method for estimating soil moisture from ERS scatterometer and soil data," *Remote Sens. Environ.*, vol. 70, no. 2, pp. 191–207, Nov. 1999.

[16] N. Pierdicca, L. Pulvirenti, A. Santarelli, R. Crapolicchio, M. Talone, and S. Puca, "Comparison of microwave passive and active observations of soil moisture," in *Proc. IEEE IGARSS Conf.*, 2012, pp. 738–741.

[17] W. Wagner, K. Scipal, C. Pathe, D. Gerten, W. Lucht, and B. Rudolf, "Evaluation of the agreement between the first global remotely sensed soil moisture data with model and precipitation data," *J. Geophys. Res.*, vol. 108, no. D19, pp. 4611-1–4611-17, Oct. 2003.

[18] M. Spencer, C. Wu, and D. Long, "Improved resolution backscatter measurements with the SeaWinds pencil-beam scatterometer," *IEEE Trans. Geosci. Remote Sens.*, vol. 38, no. 1, pp. 89–104, Jan. 2000.

[19] R. West, "Algorithm Theoretical Basis Document (ATBD): SMAP Level 1 Radar Data Products," Jet Propulsion Lab., Calif. Inst. Technol., Pasadena, CA, USA, Tech. Rep. Initial Release, v. 1, 2012.

[20] R. Joyce, J. Janowiak, A. Arkin, and P. Xie, "CMORPH: A method that produces global precipitation estimates from passive microwave and infrared data at high spatial and temporal resolution," *J. Hydrometeorol.*, vol. 5, no. 3, pp. 487–503, Jun. 2004.

[21] K. Williams and R. Greeley, "Radar attenuation by sand: Laboratory measurements of radar transmission," *IEEE Trans. Geosci. Remote Sens.*, vol. 39, no. 11, pp. 2521–2526, Nov. 2001.

[22] A. Elsherbini and K. Sarabandi, "Mapping of sand layer thickness in deserts using SAR interferometry," *IEEE Trans. Geosci. Remote Sens.*, vol. 48, no. 9, pp. 3550–3559, Sep. 2010.

Kaighin Alexander McColl (S'09) received the B.Eng.(Hons) degree in environmental engineering and the B.Sc. degree in applied mathematics from the University of Melbourne, Melbourne, Australia, in 2009. He is currently working toward the Ph.D. degree in the Department of Civil and Environmental Engineering, Massachusetts Institute of Technology, Cambridge, MA, USA.

He is funded by the National Science Foundation's Graduate Research Fellowship Program. His research interests lie in boundary-layer meteorology, land–atmosphere interactions, and remote sensing of soil moisture and vegetation.

Dara Entekhabi (M'04–SM'04) received the Bachelor's and Masters' degrees from Clark University, Worcester, MA, USA, in 1983, 1984, and 1987, respectively, and the Doctoral degree from the Massachusetts Institute of Technology (MIT), Cambridge, MA, USA, in 1990.

He is currently a Professor with the Department of Civil and Environmental Engineering and the Department of Earth, Atmospheric, and Planetary Sciences, MIT. He is the Science Team Lead for NASA's Soil Moisture Active Passive mission, which is due to launch in October 2014. His research activities are in the fields of terrestrial remote sensing, data assimilation, and coupled land–atmosphere systems modeling.

Prof. Entekhabi is a Fellow of the American Meteorological Society and the American Geophysical Union.

María Piles (S'05–M'11) was born in Valencia, Spain, in 1982. She received the M.S. degree in telecommunication engineering from the Universitat Politecnica de València, València, in 2005 and the Ph.D. degree in telecommunication engineering from the Universitat Politecnica de Catalunya (UPC), Barcelona, Spain, in 2010.

In 2008, she was a Visiting Ph.D. Student with the Department of Civil and Environmental Engineering, Massachusetts Institute of Technology, Cambridge, MA, USA, where she worked on a downscaling algorithm to combine both active and passive microwave measurements from the National Aeronautics and Space Administration Soil Moisture Active Passive mission into high-resolution soil moisture estimates. In 2010, she was as a Research Fellow with the Department of Civil and Environmental Engineering, University of Melbourne, Melbourne, Australia, where she worked on European Space Agency SMOS soil moisture validation and downscaling. Since 2011, she has been a Research Scientist with UPC and SMOS Barcelona Expert Center. She has authored/coauthored 12 papers in peer-reviewed journals and more than 60 international conference presentations. Her research activity is centered in remote sensing for Earth observation, with special emphasis on interferometric radiometry, radar and visible/infrared sensors, soil moisture retrieval algorithms, pixel disaggregation techniques, and data fusion.

Dr. Piles is currently the Secretary of the IEEE Geoscience and Remote Sensing Society Spanish chapter. She was the recipient of the Med-Storm Prize for Young Researchers in the Plinius Conference in 2011 and the UPC Special Doctoral Award in Information Technology and Communication in 2012.